



Deposited via The University of Leeds.

White Rose Research Online URL for this paper:

<https://eprints.whiterose.ac.uk/id/eprint/225308/>

Version: Accepted Version

Article:

Song, B., Li, Y., Wei, J. et al. (2025) Enhancing the impact performance of TaNbHfZr high-entropy alloy film by interface strengthening and stress dispersion: Microstructure and mechanism. *Materials Today Communications*, 44. 112127. ISSN: 2352-4928

<https://doi.org/10.1016/j.mtcomm.2025.112127>

This is an author produced version of an article published in *Materials Today Communications*, made available under the terms of the Creative Commons Attribution License (CC-BY), which permits unrestricted use, distribution and reproduction in any medium, provided the original work is properly cited.

Reuse

This article is distributed under the terms of the Creative Commons Attribution (CC BY) licence. This licence allows you to distribute, remix, tweak, and build upon the work, even commercially, as long as you credit the authors for the original work. More information and the full terms of the licence here:

<https://creativecommons.org/licenses/>

Takedown

If you consider content in White Rose Research Online to be in breach of UK law, please notify us by emailing eprints@whiterose.ac.uk including the URL of the record and the reason for the withdrawal request.

1 **Enhancing the impact performance of TaNbHfZr high-**
2 **entropy alloy film by interface strengthening and stress**
3 **dispersion: Microstructure and mechanism**

4 Baorui Song^{a, b}, Yanhuai Li^c, Jiahong Wei^{a, b}, Dan Qian^c, Liuquan Yang^d,
5 Zhongxiao Song^c, Weihua Li^{a, b, e, *}

6 ^a Henan Academy of Sciences, Zhengzhou 450046, Henan, P.R. China

7 ^b Institute of Chemistry, Henan Academy of Sciences, Zhengzhou 450046,
8 Henan, P.R. China

9 ^c State Key Laboratory for Mechanical Behavior of Materials, Xi'an
10 Jiaotong University, Xi'an 710049, Shaanxi, P.R. China

11 ^d Institute of Functional Surfaces, School of Mechanical Engineering,
12 University of Leeds, Leeds LS2 9JT, United Kingdom

13 ^e North China University of Water Resources and Electric Power,
14 Zhengzhou 450046, Henan, P.R. China

15 * Authors to whom correspondence should be addressed.

16 Email:

17 Weihua Li: liweihua1928@163.com

18 **Keywords:** High-entropy Alloy Film; TaNbHfZr; Sandwich-structure; Nano-
19 impact; Microstructure; Mechanism

20 **Abstract**

21 The sandwich-structured TaNbHfZr refractory high-entropy alloy film
22 (RHEAF) was fabricated by magnetron sputtering. Nano-impact was
23 utilized to extract the local mechanical response of the film with severe
24 localized strain due to the high instantaneous strain rate (*ISR*). Analysis on
25 dynamic hardness (H_D) and toughness of TaNbHfZr film was carried out
26 quantitatively. The plasticity absorption ability in nano-impact is higher
27 indicated by the increased plastic work (W_p) with increasing acceleration

1 force (AF). The decreased H_D is attributed to the contribution of the energy
2 to the fracture at higher AF . Through TEM observation, the dynamic
3 response is confirmed by thickness reduction in nano-impact. Cracks
4 occur where the stress reaches its maximum in the middle layer, near the
5 middle-bottom boundary, serving as the primary energy-storage
6 mechanism in the sandwich-structured TaNbHfZr film. Furthermore, the
7 rate-controlling response can be attributed to the dislocation motion at
8 varying loading rates. This phenomenon is confirmed by FEM simulation.
9 Here, the equiaxed grains within the middle layer mitigate further
10 catastrophic damage by absorbing the localized and concentrated stress
11 through rotation or grain boundary sliding. Consequently, the film was
12 strengthened and stabilized due to the effective stress dispersion and
13 existence of interface in the sandwich structure.

14 **1 Introduction**

15 High-entropy alloys (HEAs), as a fundamentally new alloying concept, has
16 been firstly proposed by Yeh *et al.* [1] in 2004. HEAs have high
17 configurational entropies at a random state ($\geq 1.5R$, R is the ideal gas
18 constant), which can stabilize the simple crystal structure by forming solid
19 solutions such as fcc (face-centered cubic) and bcc (body-centered cubic)
20 solid-solution structures, rather than complex intermetallic phases [2]. The
21 high-entropy and severe lattice distortion effects lead to a rugged energy
22 landscape which increases the resistance to dislocation motion and
23 pronounced solid solution strengthening for HEAs [3, 4]. Compared with
24 traditional refractory metals and alloys, HEAs pave a new way for an
25 excellent combination of superior functional properties, which have great
26 potential for practical applications. HEAs composed of high melting-point
27 elements such as Cr, Hf, Mo, Nb, Ta, W, Zr *etc.* named refractory high-
28 entropy alloys (RHEAs), exhibiting outstanding strength and exceptional
29 oxidation resistance [5, 6]. The reported RHEAs with bcc structure such as

1 WNbMoTa, WNbMoTaV [5], Hf₂₅Nb₂₅Ti₂₅Zr₂₅ [7], HfMo_xNbTaTiZr [8]
2 possess superior mechanical performance. Feng *et al.* [9] have prepared
3 NbMoTaW films via magnetron sputtering and reported its superior
4 nanoindentation hardness (~16 GPa) due to the source strengthening and
5 solid solution hardening mechanisms using a thermally activated
6 dislocation model.

7 The mechanism of plastic deformation is usually recognized to be rate-
8 dependent. Definitely speaking, quasi-static and dynamic high strain rate
9 conditions fall into the strain rate range of 10⁻⁵~10⁻¹ s⁻¹ and >5×10¹ s⁻¹,
10 respectively [10]. The dynamic performance of the HEAFs is often
11 involved in practical applications such as high-speed transportation
12 vehicles and hydraulic machinery *etc.* [11]. Nano-impact makes it possible
13 to quantify energy absorption of a material surface in nano-/micro-scale
14 and provides valuable highly localized information about deformation
15 acting as an effective measurement of impact energy to determine the
16 fracture resistance [12].

17 As evidenced by Gray and Hirsch *et al.* [13, 14], the dislocation structures
18 are substantially different between low strain rate and high strain rate via
19 TEM (transmission electron microscopy) micrographs. The rate-
20 dependence for bcc metals suggests that the deformation occurs via
21 thermally activated kink-pair nucleation which is a typical screw dislocation
22 propagation mechanism [15]. Twinning and shear bands related
23 deformation mechanisms are proposed at lower strain rates and softening
24 even occurs at higher strain rates. Nemat-Nasser *et al.* [16] reported that
25 phenomena like shear bands, dynamic recovery, dislocation lines,
26 dislocation forests and deformation dislocation loops arise in the dynamic
27 deformation with strain rate >5×10⁴ s⁻¹ for bcc Ta, as well as slip of the
28 perfect screw dislocations on {110}-type primary planes as the dominant
29 deformation mechanism, which are confirmed via TEM analysis. The yield

1 strength of as-cast TiHfZrTaNb HEA at the initial strain rates $\sim 3.4 \times 10^3 \text{ s}^{-1}$
2 with localized in macroscopic shear bands was about $\sim 40\%$ higher than
3 that measured at $\sim 10^{-3} \text{ s}^{-1}$ with evenly distributed shear bands by
4 compression due to the increase of the dislocation density [17]. The
5 dynamic fracture often emerges as one type of the phenomena during the
6 overall process of a target impacted by a projectile [18]. While for
7 nanocrystalline and ultrafine bcc V, shear banding rather than crack
8 initiation and propagation is observed with promoting shear localization in
9 dynamic compression with strain rate of $\sim 10^3 \text{ s}^{-1}$ [19].
10 However, RHEAs always exhibit apparent brittleness and lack of room-
11 temperature ductility, which remains major and important challenges for
12 their processing and application [20]. Combining the ductile material with
13 the hard one to coordinate the comprehensive excellent performance of
14 RHEAs is meaningful and necessary. Zhao *et al.* [21] prepared a
15 Cu/(NbMoTaW) nanolaminates introducing the hard NbMoTaW HEA
16 laminates into the soft Cu to form the ultra-strong Cu/HEA composites.
17 Besides, as reported by Wei *et al.* [20], the TiVNbHf RHEA gets more
18 ductile with higher fracture elongation due to the evolution to fully
19 equiaxed grain after homogenization. Herein, we developed a body-
20 centered cubic (bcc) sandwich-structured TaNbHfZr film. This designed
21 film integrates exceptional ductility of the middle layer characterized by
22 equiaxed grains, with enhanced resistance to softening in the upper and
23 lower layers which feature columnar grains. We evaluated the mechanical
24 behavior of magnetron-sputtered TaNbHfZr RHEAF in terms of the high
25 strain rate hardness H_b by nano-impact and also bridge the correlation of
26 the plasticity and toughness under test conditions with different strain
27 rates. At the same time, we introduce the energy-related evaluation to
28 discuss the plasticity evolution during the dynamic impact deformation as
29 well as the corresponding mechanisms.

2 Materials and Methods

2.1 Film deposition and characterization

The TaNbHfZr target ($\phi 75 \times 5$ mm) was prepared via powder metallurgy with purities higher than 99.99% and was nominally equiatomic ($\text{Ta}_{25}\text{Nb}_{25}\text{Hf}_{25}\text{Zr}_{25}$). The (100) Si wafer substrates were cleaned ultrasonically in acetone, absolute ethyl alcohol and deionized water sequentially before deposition. The base pressure of the vacuum system during deposition via magnetron sputtering (JPG450a dual-chamber magnetron sputtering deposition system) was less than 1×10^{-4} Pa. The deposition process was conducted by DC source in an argon atmosphere with a target power of 200 W. The Ar flow rate was maintained at 25 sccm, and the working pressure was 0.4 Pa. The substrate bias was set at -100 V with substrate heating to 700 °C before the deposition. To achieve the layered structure, the film was initially deposited at 700 °C for 18 mins, marked as stage 1; followed by a 12-minute interruption of the heating process, marked as stage 2. Subsequently, the heater was reactivated for an additional 30 mins, marked as stage 3. During the whole process, the entire deposition was continuous, with only the substrate temperature being changed, and the total deposition time was 60 mins. The finer columnar grains in the lower layer were obtained at stage 1, the equiaxed grains in the middle layer were obtained at stage 2, and the coarser columnar grains in the upper layer were obtained at stage 3.

The phase structure of the TaNbHfZr film was characterized with Cu K α radiation on a Bruker D8 discover powder X-Ray diffractometer at room temperature, at a scan speed of 2°/min from 10°-120°. Scanning electron microscopy (SEM, FEI-VERIOS460) was employed to observe the surface morphologies. High-resolution transmission electron microscopy (HR-TEM, JEM-2100F) experiment was conducted to observe and determine the

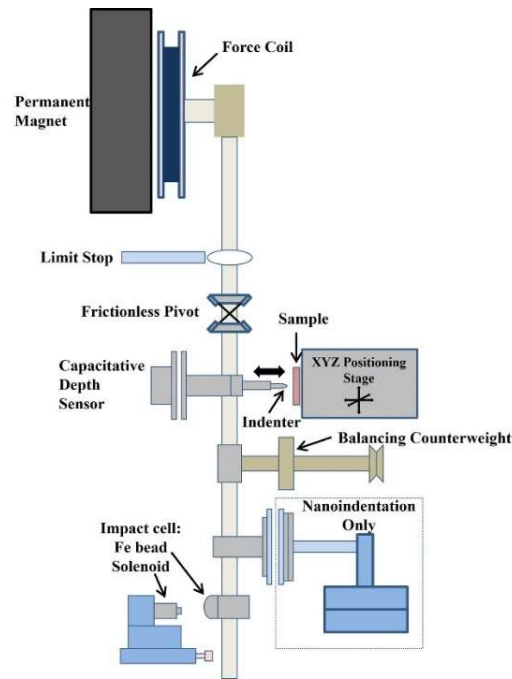
1 cross-sectional microstructure of the TaNbHfZr film, as well as the
2 elemental composition via energy dispersive X-Ray spectroscopy (EDS)
3 analysis. The atomic force microscope (AFM, INNOVA) was used to
4 analyze the surface roughness of these films.

5 The TEM foil for deformed specimen of nanoindentation at load=50 mN
6 with $LR=0.5$ mN/s and nano-impact at $AF=5$ mN were prepared using the
7 Helios G4 CX FIB (Focused Ion Beam) workstation. 30 KeV was used to
8 lift out the cross-section sample from one corner to the opposite side of
9 the indentation imprint. The coarse and fine milling was performed at the
10 current from 0.79 nA, 0.43 nA, 0.23 nA to 80 pA. Low-energy cleaning was
11 then performed at 5 KeV and 2 KeV after the milling. The TaNbHfZr pillars
12 were prepared using FIB with diameter of 400 nm and height/diameter
13 ratio of 2.5.

14 **2.2 Nanomechanical tests**

15 The nano-impact and nanoindentation experiments were carried out in a
16 controlled environment (25 °C and 65% relative humidity) using a
17 NanoTest Vantage system (Micro Materials Ltd, Wrexham, UK). A
18 calibrated diamond Berkovich indenter with a nominal tip curvature radius
19 of ~50 nm was utilized for nano-impact and nanoindentation tests. The
20 area function of the indenter was calibrated based on measurements from
21 a fused silica reference sample. The apparatus of nano-impact is
22 illustrated in **Figure 1**. For the nano-impact test, the AF was set at 5, 15
23 and 30 mN. The indenter was positioned at an accelerated distance (AD)
24 of 15 μm from the sample. The loading coil current was maintained
25 constant throughout the impact. As a result, the kinetic energy (KE) of the
26 pendulum increased until contact occurred, and the indenter reached its
27 maximum penetration depth in the sample before rebounding. The
28 indenter ultimately settled on the surface after several “bounces”. The
29 plastic deformation was completed in the first cycle, rendering the

1 influence of subsequent rebounds on the final impression depth
2 insignificant [22]. The effective pendulum mass was 210 g. Owing to the
3 flat and smooth surface of the TaNbHfZr film, each nano-impact at an AF
4 was repeated 3 times with a 50 μm interval. The residual contact area of
5 the nano-impact at $AF=5$, 15 mN was measured using Image-J software.



6

7 **Figure 1** Schematic diagram of experimental apparatus used to quantify
8 the impact response (referred and modified from ref. [13])

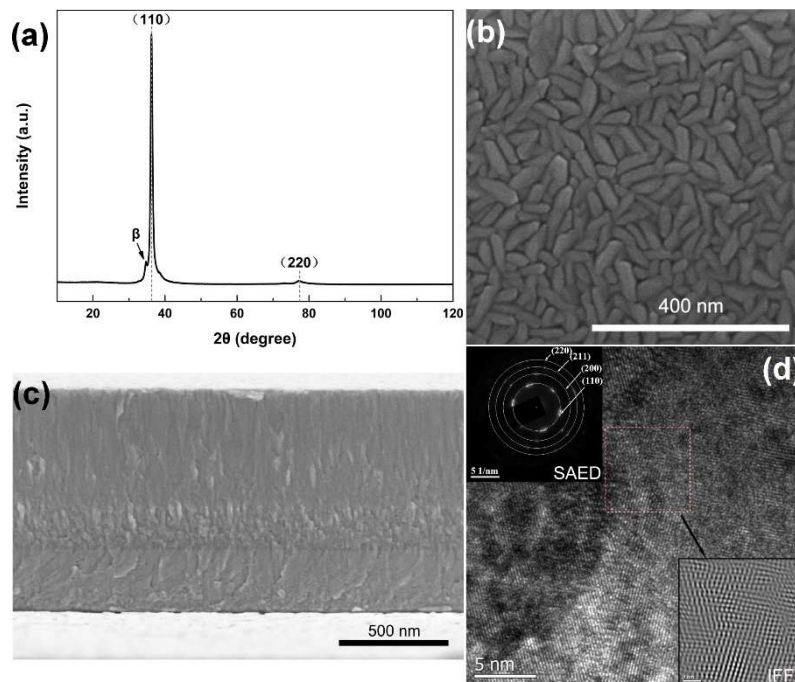
9 **2.3 FEM modeling of cracking**

10 The mechanical model was constructed in a 2D axisymmetric framework,
11 simulating a plane-strain state. The system employed a four-node bilinear
12 plane strain quadrilateral element (CPE4R) governed by reduced
13 integration and hourglass control. During the indentation process, the
14 mesh was refined to a size of 50 nm. The indenter was conceptualized as
15 analytical rigid body, and its conico-spherical profile was designed to fit the
16 area shape function $A(h)$ of a Berkovich indenter (where $A(h)$ is the
17 indenter section at a distance h from the tip apex). The opening angle of

1 the indenter was 70.32° . The simulation cell was taken sufficiently wide to
2 prevent the stress/strain fields generated within the sample during
3 indentation from interacting with the outer boundary. Additionally, a $5\ \mu\text{m}$
4 thickness for the silicon substrate within the computational cell was
5 deemed adequate. The crack propagation was implemented using a
6 coupled Cohesive Zone Model (CZM), and the crack openings followed
7 the cohesive traction-separation law [23]. In this instance, the maximum
8 principal stress criterion was selected for crack initiation. For the
9 constructed model, the set of simultaneous non-linear dynamic equilibrium
10 equations were solved iteratively using Newton's method.

11 **3 Results and discussion**

12 **3.1 Microstructural analysis**



13

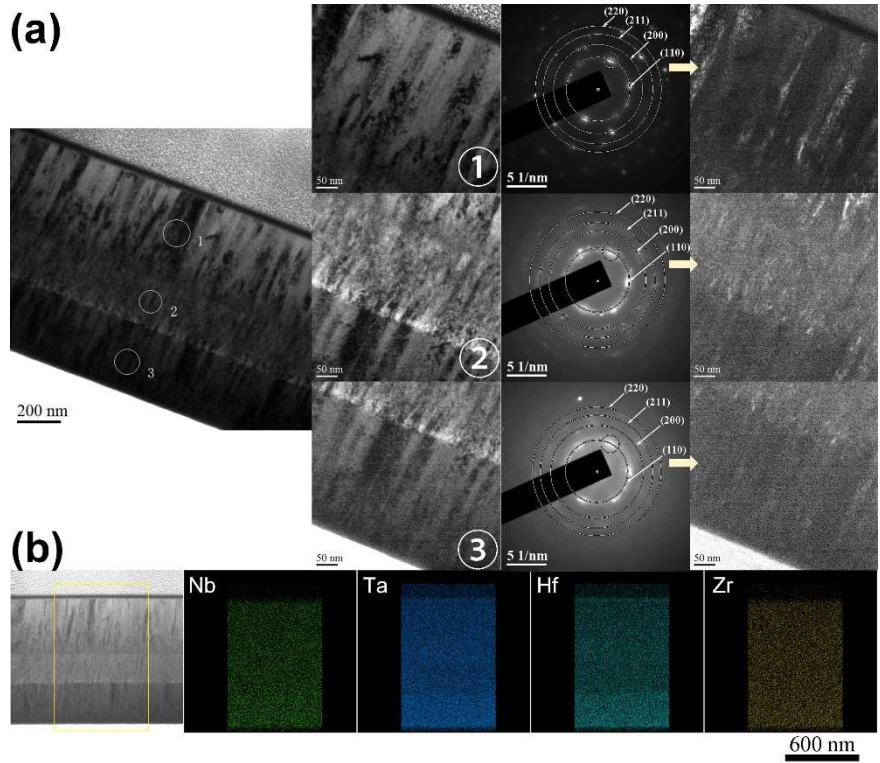
14 **Figure 2 (a)** XRD pattern; SEM image of **(b)** surface morphology; **(c)**
15 cross-sectional morphology; **(d)** HR-TEM image, inserts are the SAED
16 (Selected Area Electron Diffraction) and the IFFT (Inverse Fast Fourier
17 Transformation) images of the selected area denoted by a red dotted

1 square for the as-deposited TaNbHfZr film.

2 The XRD pattern of the as-deposited TaNbHfZr film, depicted in **Figure 2**
3 **(a)**, reveals that the primary phase structure is body-centred (bcc),
4 characterized by a dominant (110) plane at $\sim 37^\circ$. Additionally, a minor
5 secondary β hcp phase is present at $\sim 35^\circ$, as indicated in previous work
6 [24, 25]. In **Figure 2 (b)**, the top surface is characterized by needle-like
7 granules with width ranging from 30 to 40 nm. At high deposition
8 temperature, the coarsening driving force through surface atomic diffusion
9 and grain boundary movement enhances, thus the particles on the film
10 surface coalesce along preferred orientation as needle shape to reduce
11 the total surface energy and interface energy [9, 26]. Additionally, the
12 surface is densely packed and devoid of any hole. AFM analysis in **Figure**
13 **S1** shows the surface average roughness R_a is ~ 2 nm. The cross-
14 sectional morphology in **Figure 2 (c)** depicts the dense morphology and a
15 sandwich layered structure with a total thickness of 1 μm (300 nm for
16 lower columnar-grain layer, 200 nm for equiaxed-grain middle layer and
17 500 nm for upper columnar-grain layer). In addition, there is a good
18 adhesion between columnar and equiaxed grain structures, characterized
19 by clear and intact interfaces. The EDS analysis indicates that the film
20 possesses nearly equiatomic elemental compositions of Ta, Zr, Nb, Hf (25
21 at. %, 24 at. %, 29 at. % and 22 at. %, respectively). The HR-TEM
22 analysis in **Figure 2 (d)** exhibits clear and continuous lattice fringes in
23 both the HR-TEM and IFFT images. Besides, some lattice distortion can
24 be discerned due to atomic-size mismatch and elastic-modulus mismatch
25 within the average bcc lattice [27].

26

27



1

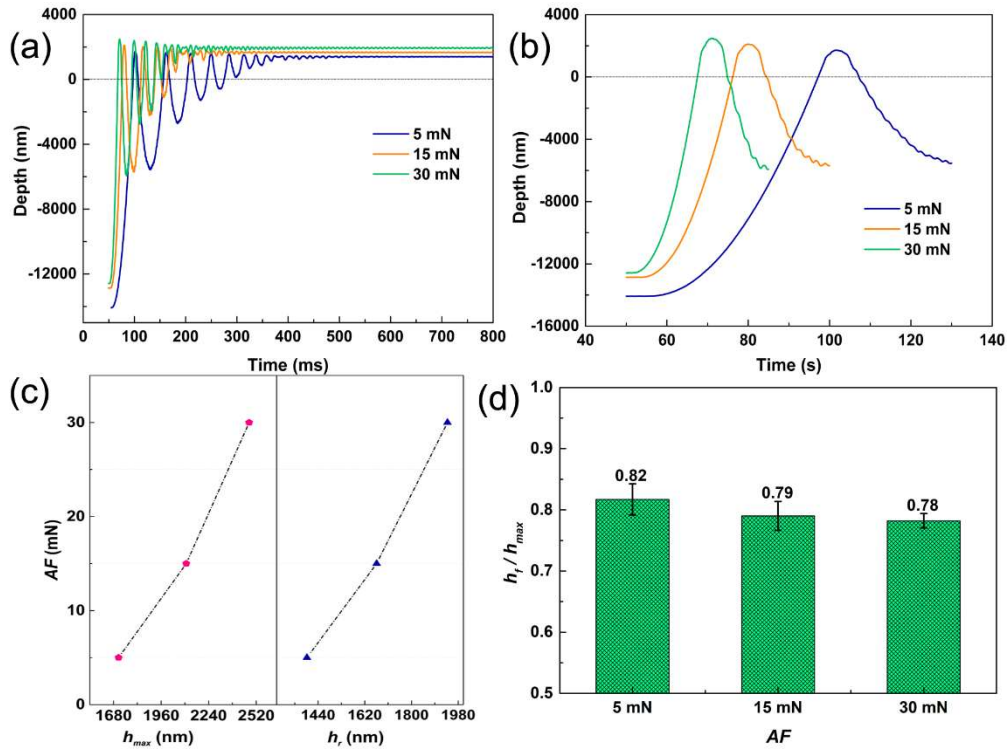
2 **Figure 3 (a)** SAED and corresponding DF (dark field) images of different
 3 layers; **(b)** EDS-mapping of elemental distribution for as-deposited
 4 TaNbHfZr film.

5 TEM analysis of the as-deposited TaNbHfZr film lifted out by FIB is shown
 6 in **Figure 3 (a)**. The distinct layered structure is characterized by
 7 elongated and coarser columnar grains extending throughout the upper
 8 layer, equiaxed grains with sizes differ little in all directions in the middle
 9 layer, and finer columnar grains in the bottom layer can be seen. SEAD
 10 images help to characterize each layer with clearly separated spots in the
 11 top layer, fine and continuous spots in the middle layer, and coarser spots
 12 compared with those in the top layer. DF images on the right specifically
 13 present the shape and size of the grains in each layer (the light part
 14 indicates the grains circled in SAED). The elemental distribution of each
 15 layer was homogeneous as demonstrated in **Figure 3 (b)**. The phase
 16 structure of three layers were identical, all keeping BCC structure with
 17 crystal plane of (110), (200), (211) and (220). At stage 1, the deposition

1 temperature (T_s) is 700 °C, and the melting point (T_m) of TaNbHfZr is
2 2385.8 °C, $T_s / T_m=0.3$. In this zone, the film is more prone to form
3 refined grains with a certain texture, thus finer columnar grains formed
4 [26]. At stage 2, the cooling effect during the temperature break-off
5 bringing increased nucleation points and nucleation points, with the high-
6 entropy and sluggish diffusion effects, as well as the heavy transition
7 elements composed in the film, lead to variations in diffusion velocity of
8 atoms during deposition. This favors the formation of refined equiaxed
9 grains in the middle layer of the film, due to increased compositional
10 undercooling [28, 29]. Besides, at lower deposition temperature, the ability
11 of atoms to migrate decreases, resulting in limited surface diffusion,
12 increased nucleation points and nucleation density, as well as decreased
13 driving force for recrystallization, which contributes to the formation of
14 equiaxed grains [30]. During the continuous deposition process,
15 compared to stage 1, stage 3 no longer needs to form nucleation sites
16 through the diffusion and rearrangement of atoms. At stage 3, a large
17 number of nucleation sites undergo significant growth and recrystallization,
18 giving rise to the formation of numerous coarser columnar grains in the
19 upper layer of the film.

1 3.2 Nano-impact

2 3.2.1 Analysis of real-time impact depth curves

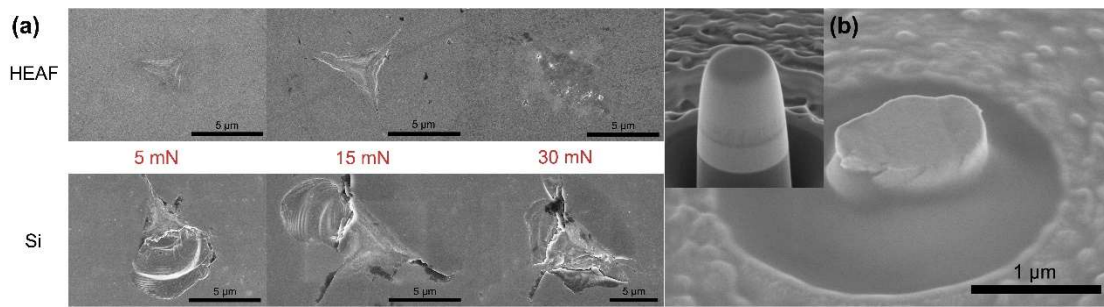


3
4 **Figure 4** (a) Typical real time-depth curves; (b) the 1st cycle depth-time
5 curves; (c) h_{max} , h_r vs. AF curves; (d) h_r/h_{max} of TaNbHfZr HEAFs for nano-
6 impact at AF=5, 15, 30 mN.

7 The typical real-time depth curves of nano-impact at AF=5, 15 and 30 mN
8 are shown in **Figure 4 (a)**, where the apparent oscillation can be seen due
9 to the dynamic compliance of the pendulum during the reciprocal loading
10 of impact. Some error may be introduced to the measurement of the
11 rebound energy and lengthening the period at the maximum depth during
12 impact [31]. The deep impact depth indicates strong dynamic response of
13 the film during impact. However, considering that most permanent
14 deformation has been completed in the 1st contact cycle, the detailed
15 energy dissipation in this cycle was examined. The contact cycle consists
16 of four phases as depicted in **Figure S2 (a)**: acceleration, indentation,
17 rebound and deceleration. As supposed, higher AF corresponds to the
18 higher h_{max} and h_r in **Figure 4 (c)**. Toughness is the ability of a material to

1 absorb energy during deformation up to fracture, while fracture toughness
2 is the ability to resist the growth of a preexisting crack [32]. We use
3 toughness here to encompass both the energy required to crack and to
4 enable the crack to propagate until fracture, including the cases from
5 lower to higher AF . The calculated h_r/h_{max} value illustrated in **Figure 4 (d)**
6 is used as the index to measure the toughness [33], where h_r denotes the
7 plastic deformation during the impact process. The results exhibit that the
8 h_r/h_{max} decreased from 0.82 to 0.78 as AF increases in nano-impact,
9 suggesting an increase in plasticity absorption.

10 3.2.2 SEM morphologies for the impact imprints and microcompression 11 pillar



12
13 **Figure 5 (a)** SEM morphologies of impact imprints for TaNbHfZr HEAF
14 and Si substrate at $AF=5, 15, 30$ mN; **(b)** the morphology of the pillar at
15 loading rate of 1 nm/s before (inset) and after compression.

16 The SEM morphologies of the impact imprints of TaNbHfZr film and Si
17 substrate are displayed in **Figure 5 (a)**. At $AF=30$ mN, the TaNbHfZr film
18 delaminated from the Si substrate, leaving a shallow imprint. In contrast,
19 uncoated Si exhibited visible radial cracks even at 5 mN, indicating that
20 the deleterious effect becomes more pronounced at higher AF . Obviously,
21 the protective film prevents the substrate from further degradation. The
22 emergence of cracks reveals that the film requires increased ductility to
23 resist cracking, fracture or spallation under dynamic impact. It has been
24 confirmed that thinner film experiences higher stresses at the film-

1 substrate interface [27, 34]. Failure mechanisms during impact can be
2 attributed to: micro-cracks initiation in the film post-impact; continued
3 nucleation, coalescence, or propagation of cracks at the film-substrate
4 interface, as indicated by minimal depth change in early impact cycles;
5 debonding at the interface due to interfacial mismatch during plastic
6 deformation and relaxation of pre-existing residual stress in the film [31,
7 35]. Microcracks form at the contact edge due to peak stress [33], which
8 can also be verified by the following FEM simulation results. Rupture
9 behavior near the film-substrate interface, observed in quasi-static micro-
10 compression tests at loading rates of 1 nm/s in **Figure 5 (b)** and 5 nm/s in
11 **Figure S3**, provides evidence of fracture phenomenon consistent with the
12 aforementioned failure mechanisms. The measured nanoindentation
13 hardness at 50 mN of Si substrate is $\sim 11.7 \pm 0.19$ GPa, and the reduced
14 modulus is $\sim 177.1 \pm 1.55$ GPa. For this harder film / softer substrate
15 system, a larger deformation of the Si substrate will occur during impact
16 when the penetration depth of the indenter reaches or deeper than the
17 film/substrate interface. Besides, the deformation of Si substrate can
18 cause the film to bend or peel off, aggravating the dynamic effect in
19 nano-impact.

20 3.2.3 Dynamic hardness

21 We use the Meyer hardness as a representation of H_D [36]

$$22 \quad H_D = \frac{P_m}{A} \quad \text{Equation 1}$$

23 For a self-similar indenter geometry, A_c can be measured from
24 microscopic observations of the impact impression, P_m represents the
25 maximum resistance force obtained at the maximum depth of contact
26 during impact, which is entirely determined by the dynamic compliance of
27 the instrument, the sample properties and the geometry and initial impact
28 energy of the indenter [37]. The proposed model, which includes the
29 motion of the pendulum and the additional resistance accompanying the

1 indenter once contact begins and increases, can be expressed
2 mathematically as [22, 38]

$$3 \quad m\vec{a} + c\vec{v} + k\vec{x} + \overline{F(x)} = \overline{AF} \quad \text{Equation 2}$$

4 where c represents the damping coefficient, primarily due to air damping.
5 k signifies the spring stiffness, \vec{x} is the indentation depth vector, and a is
6 the acceleration velocity, which can be derived from the second derivative
7 of the fitted $h-t$ curve during the indentation phase in 1st cycle impact using
8 the 5th-order polynomial fitting. As the plastic deformation was completed
9 at the initial contact, we analyzed the first cycle of impact at $AF=5$ mN
10 qualitatively. When the penetration depth approaches its maximum,
11 damping effects are considerably reduced, and hence, the resistive force
12 $F(x)$ can be approximated as

$$13 \quad F(x) = P_m \approx ma + AF \quad \text{Equation 3}$$

14 The method to obtain a and P_m is illustrated in **Figure S2. (b)**. The
15 theoretical H_D can be derived using **Equation 1-3**, with the results
16 summarized in **Table 1**. Based on the one-dimensional model proposed
17 by Andrews and Constantinides *et al.* [38, 39], the H_D of aluminum 1100
18 measured by nano-impact was slightly higher than its static hardness.
19 While the dynamic hardness experiences obvious reduction when fracture
20 occurs. The contribution of the energy transfers from plastic deformation
21 to crack or fracture so that the resistance for the plastic deformation
22 weakens and correspondingly the hardness decreases sharply. The
23 calculated H_D is higher at $AF=5$ mN with 8.57 GPa to 7.09 GPa at $AF=15$
24 mN in dynamic nano-impact without considering the energy dissipation in
25 cracks and fracture. This can be explained by the strain gradient plasticity
26 (*SGP*) theory that dislocation density increases at decreased loads
27 caused by the presence of *GND* [22, 40, 41].

28

29

1 **Table 1** The calculated result of nano-impact at $AF=5, 15$ mN.

AF (mN)	H_D (GPa)	W_P (nJ)	ΔE (nJ)	U_{fra} (nJ)
5	8.57	18.80	22.79	3.99
15	7.09	40.38	87.11	46.72

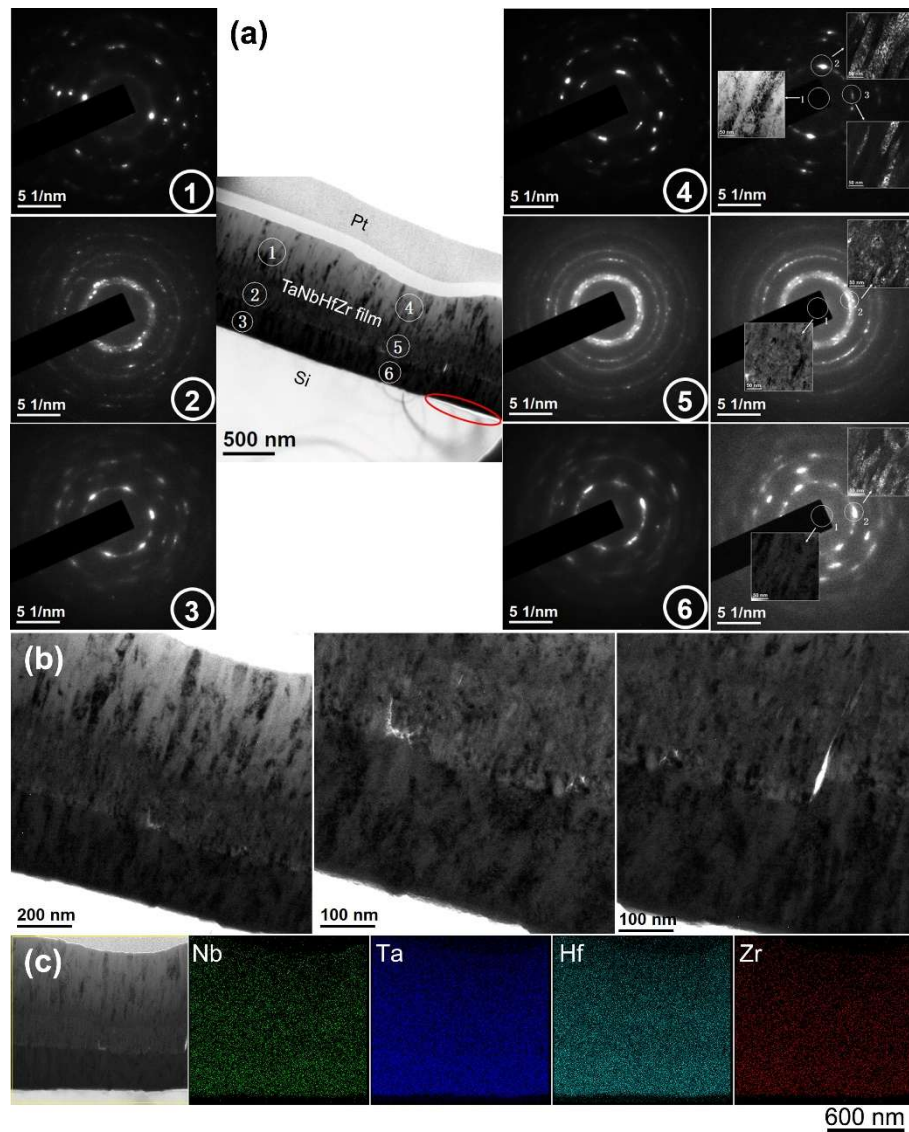
2 **3.2.4 Impact energy**

3 The energy loss during acceleration is estimated to be approximately 44.7
 4 % due to energy dissipation in the system from damping and friction [35,
 5 37]. The effective acceleration transfer work increases with AF [42]. For
 6 simplicity, we have omitted the thermal energy and damping effect
 7 induced energy loss. As shown in **Table 1**, the contribution to the fracture
 8 part also increases from 3.99 nJ of 5 mN to 46.72 nJ of 15 mN, exhibiting
 9 the apparent rate-dependent behavior. The kinetic energy difference (ΔE)
 10 can be equivalently considered as the sum of the (W_P) and fracture work
 11 (U_{fra}). Specifically, it is assumed that all the fracture work is absorbed by
 12 the film only. W_P is calculated using Tabor's method [36]. To determine
 13 U_{fra} , we introduce the following relationship

14
$$U_{fra} = 0.553\Delta E - W_P = 0.2765m(v_{in}^2 - v_{out}^2) - \frac{1}{3}A_P h_r H_D$$
 Equation 4

15 where the effective mass of the pendulum is denoted as m , with a value of
 16 0.21 kg. v_{in} represents the initial velocity before the indentation of the
 17 indenter, v_{out} denotes the outgoing velocity at the point where the tip
 18 detaches from the sample on the initial rebound, A_P is the projected
 19 contact area of the indenter. The calculated results are summarized in
 20 **Table 1**. For impact at $AF=5$ mN of TaNbHfZr film, the energy contribution
 21 to U_{fra} accounts for 17.5% of the kinetic energy difference, which is the
 22 primary factor that makes the H_D much smaller than the hardness in
 23 quasi-static circumstances, as shown in **Table S1**.

1 3.2.5 Microstructure characterization by TEM of impact-deformed film



2
3 **Figure 6 (a)** SAED image of the areas located beyond (area ①, ② and ③)
4 and directly below (area ④, ⑤ and ⑥) the indenter, specific spots in the
5 SEAD images indicate the BF (marked “1”) and DF (marked “2” and “3” for
6 area ④, marked “2” for area ⑤ and ⑥) images; a delamination gap
7 between the TaNbHfZr film and Si substrate is highlighted by a red circle;
8 **(b)** Cracks in the middle layer near the interface; **(c)** Homogeneous
9 elemental distribution by TEM-EDS mapping of the deformed area
10 throughout the TaNbHfZr film after impact deformation at $AF=5$ mN.
11 Six sites away from (①, ②, ③) and right below (④, ⑤, ⑥) the indenter are
12 selected to elucidate the microstructural change after impact at 5 mN. As

1 illustrated in **Figure 6 (a)**, a preferred orientation of the lattice plane is
2 clear and distinct in site ④, which is analogous to that of the as-deposited
3 sample; in site ⑤, dense and continuous spots are connected nearly into
4 separated rings in SAED with visible cracks at the bottom of this zone,
5 enlarged in **Figure 6 (b)**; while in site ⑥, visibly fuzzy and elongated
6 diffraction spots suggest a distorted lattice plane towards various
7 directions, rather than a preferred orientation as seen in the as-deposited
8 film. The grain size of the upper layer ranges of 20 to 50 nm, which is less
9 homogeneous than that of the as-deposited film with a range of 30 to 40
10 nm; and the grains exhibit a growth direction nearly identical to that of the
11 as-deposited film. The microstructure remains unchanged away from the
12 indenter compared with the as-deposited film. In the deformed area, the
13 extent of deformation is described by the layer thickness change of middle
14 layer: compared with the as-deposited film, the reduction of thickness of
15 the middle layer in nanoindentation at 50 mN was ~9 nm as depicted in
16 **Figure S4**, and ~56 nm in nano-impact at 5 mN. This larger thickness
17 reduction suggests a dynamic response in high-strain-rate nano-impact.
18 During the impact, the stress distribution is inhomogeneous in the
19 deformed area. Typically, the zone of intense plastic deformation is
20 relatively confined and is limited to a region close to the impact surface
21 [31]. Concurrently, since the absolute value of the tensile stress in the
22 interface center is larger than it for the compressive stress in the surface
23 center [43, 44], the region below the indenter in the film-substrate interface
24 experiences tensile stress, causing the film to bend upwards. This
25 phenomenon can be confirmed from the visible delamination gap shown in
26 **Figure 6 (a)**, marked with red circle. The maximum rebound force,
27 combined with the upward tensile stress and the downward compressive
28 stress induced by the indenter, results in the stress concentration in the
29 middle layer. While at the interface between the middle and bottom layers,

1 stress cannot be released promptly due to the complex collaborative
2 deformation of the columnar grains in the bottom layer. The dispersion of
3 stress during dynamic deformation is evident, which can be further
4 confirmed by the subsequent FEM simulation.

5 Large quantities of grain boundaries are present in the middle layer, with
6 equiaxed grains deforming via rotating or grain boundary sliding. This
7 process involves grain boundary dislocations and boundary migration [45]
8 to coordinate and withstand the most severe plastic deformation,
9 strengthening and preventing the entire film from through-thickness crack,
10 fracture or spallation from the substrate. In the bottom layer, the columnar
11 grains become distorted with disordered orientation due to plastic
12 deformation, resulting in fuzzy and elongated spots on the diffraction rings.
13 In contrast, grain distortion occurs in the top layer in quasi-static plastic
14 deformation (**Figure S4**), while it happens in the bottom layer during
15 dynamic deformation. The change in the deformation zone may also be a
16 product of rate-dependent deformation. The EDS mapping result in **Figure**
17 **6 (c)** illustrates homogeneous element distribution without segregation or
18 precipitation, notably, this lamination structure maintains its composition
19 even under dynamic impact deformation. Generally, energy loss is equal
20 to the energy stored in the material. Energy-storage mechanisms include
21 crack generation, pore collapse, phase transformations interfacial defects,
22 and frictional processes such as sliding of crack surfaces and dislocations
23 motion [18]. In this study, the TaNbHfZr film loses or stores energy by
24 forming cracks. The amount of the energy can be measured using the
25 fracture energy U_{fra} , as listed in **Table 1**.

1 any stacking fault energy, minus the work done by the applied stress [49].
2 This can be mathematically expressed by

$$3 \quad G = 2\pi r_c W + \pi r_c^2 \gamma - \pi r_c^2 b \sigma \quad \text{Equation 7}$$

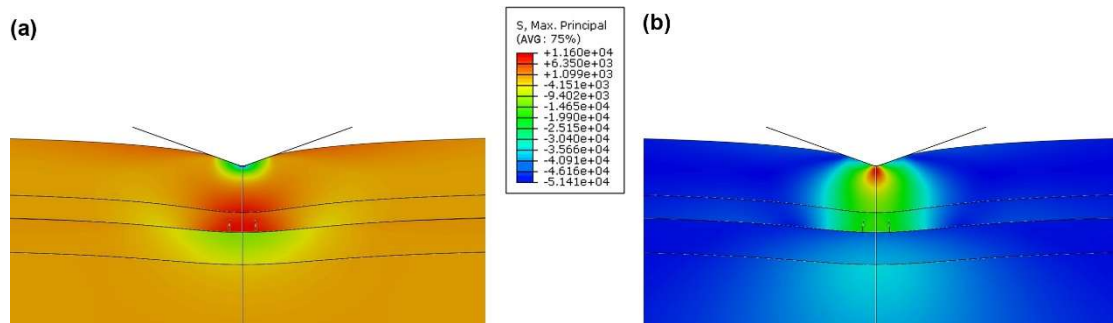
4 where r_c is the critical radius of a dislocation loop, γ represents the
5 stacking fault energy, b is the Burgers vector of the dislocation, and σ is
6 the applied stress. It is indicated that an increase in the applied stress σ
7 can effectively reduce G and consequently increase J_c .

8 During impact, the force of inertia can significantly increase the contact
9 force, resulting in a higher density of dislocation nucleation. At higher LR ,
10 the film subjected to the indenter experiences higher stress within a unit
11 time, leading to more dislocations near the deformation area. Generally,
12 solute-solution interaction dominates the kinetics of deformation at low
13 flow stress levels, while at higher stress levels, dislocation-dislocation
14 interaction dominates crystal rheology [50]. The deformation mechanism
15 of the nanocrystalline TaNbHfZr film with abundant grain boundaries is
16 dominated by the dislocation-dislocation interaction at higher AF with
17 higher strain rate. As the density of dislocation increases at higher strain
18 rates, deformation becomes tougher, providing evidence of the rate-
19 dependent behavior of TaNbHfZr film at dynamic deformation.

20 **3.4 Simulation of stress distribution in the film**

21 FEM simulation was conducted to further confirm the stress distribution
22 within the sandwich-structured TaNbHfZr film. The simulation results
23 indicate that cohesive cracking occurs within the middle layer adjacent to
24 the indentation loading axis. As shown in **Figure 8**, which illustrates the
25 maximum principal stress distribution, it is evident that the topmost
26 indented region experiences significant compressive stress, while the
27 bottom portion undergoes bending tensile stress. The middle layer,
28 situated near the loading axis, is predominantly subject to tensile stress

1 throughout the layer. This phenomenon is determined by the structure of
 2 the three-layer system, and the cracking mechanism can be deduced to
 3 be driven by the coupling effect of bending tensile and shear stress.
 4 Moreover, the upper surface of the bottom layer is under compression due
 5 to the extensive overlying pressure from the middle layer, a situation partly
 6 attributable to the higher stiffness (modulus) of the bottom layer compared
 7 to the middle one. The simulation results of stress distribution in **Figure 8**
 8 well matches and elucidates the indentation-induced damage behavior
 9 within the sandwich-layered system with the impact-deformed
 10 microstructure in **Figure 6**, where crack events occur when the stress in
 11 the middle layer, near the middle-bottom boundary, attains its maximum
 12 value.



13

14 **Figure 8 (a)** Maximum principal and **(b)** Mises stress distribution of
 15 TaNbHfZr film after nanoindentation at 50 mN.

16 **4. Conclusions**

17 The sandwich-structure TaNbHfZr film exhibits rate-dependent behavior
 18 during dynamic nano-impact. Cracks are the primary energy-storage
 19 mechanism. W_p and U_{fra} increase with strain rates at higher AF , and
 20 cracks emerge in the middle layer where stress concentrates. The
 21 decreased H_D can be explained by the increased energy contribution to
 22 fracture at higher strain rates during nano-impact. The equiaxed grains
 23 within the middle layer deform through rotation or grain boundary sliding,

1 thereby accommodating and withstanding the most severe plastic
2 deformation. This process effectively prevents the film from experiencing
3 through-thickness cracking, fracturing, or spallation from the substrate in
4 that the stress was dispersed by interfaces in the sandwich structure.

5 Examination of the microstructure and the mechanism of dynamic nano-
6 impact of the sandwich-structured TaNbHfZr film provides insights into the
7 overall mechanical performance at nano-scales. This understanding offers
8 valuable evidence and design strategies for materials, particularly
9 refractory high entropy alloy films, when subjected to equivalent high-
10 strain-rate service conditions.

11 **CRedit authorship contribution statement**

12 **Baorui Song**: Writing – Original draft, Investigation, Conceptualization,
13 Formal analysis, Data curation. **Yanhui Li**: Conceptualization, Methodology,
14 Writing – review & editing, Validation. **Jiahong Wei**: Investigation. **Dan Qian**:
15 Formal analysis. **Liuquan Yang**: Conceptualization, Visualization. **Zhongxiao**
16 **Song**: Resources, Software. **Weihua Li**: Project administration, Resources,
17 Supervision, Funding acquisition.

18 **Declaration of Competing Interest**

19 The authors declare that they have no known competing financial interests
20 or personal relationships that could have appeared to influence the work
21 reported in this paper.

22 **Data availability**

23 Data will be made available on request.

24 **Acknowledgements**

25 This work was supported by the Joint Fund of Henan Province Science
26 and Technology R&D Program (225200810090), the Key R&D and

1 Promotion Project of Henan Province (Science and Technology Research)
2 (232102230039), the Research Start-up Fund of Henan Academy of
3 Sciences (231818023), and the Fundamental Research Fund of Henan
4 Academy of Sciences (230618028).

5 **References**

- 6 [1] J.W. Yeh, S.K. Chen, S.J. Lin, J.Y. Gan, T.S. Chin, T.T. Shun, C.H. Tsau, S.Y.
7 Chang, Nanostructured high-entropy alloys with multiple principal elements:
8 novel alloy design concepts and outcomes, *Adv. Eng. Mater.* 6(5) (2004) 299-
9 303.
- 10 [2] W. Zhang, P.K. Liaw, Y. Zhang, Science and technology in high-entropy alloys,
11 *Sci. China Mater.* 61(1) (2018) 2-22.
- 12 [3] W.L. Hsu, C.W. Tsai, A.C. Yeh, J.W. Yeh, Clarifying the four core effects of
13 high-entropy materials, *Nat. Rev. Chem.* 8(6) (2024) 471-485.
- 14 [4] E. Ma, X. Wu, Tailoring heterogeneities in high-entropy alloys to promote
15 strength-ductility synergy, *Nat. Commun.* 10(1) (2019) 5623.
- 16 [5] O.N. Senkov, G.B. Wilks, D.B. Miracle, C.P. Chuang, P.K. Liaw, Refractory
17 high-entropy alloys, *Intermetallics* 18(9) (2010) 1758-1765.
- 18 [6] W. Xiong, A.X.Y. Guo, S. Zhan, C.T. Liu, S.C. Cao, Refractory high-entropy
19 alloys: A focused review of preparation methods and properties, *J. Mater. Sci.*
20 *Technol.* 142 (2023) 196-215.
- 21 [7] Y.D. Wu, Y.H. Cai, X.H. Chen, T. Wang, J.J. Si, L. Wang, Y.D. Wang, X.D. Hui,
22 Phase composition and solid solution strengthening effect in TiZrNbMoV high-
23 entropy alloys, *Mater. Des.* 83 (2015) 651-660.
- 24 [8] C.C. Juan, K.K. Tseng, W.L. Hsu, M.H. Tsai, C.W. Tsai, C.M. Lin, S.K. Chen,
25 S.J. Lin, J.W. Yeh, Solution strengthening of ductile refractory HfMo x
26 NbTaTiZr high-entropy alloys, *Mater. Lett.* 175 (2016) 284-287.
- 27 [9] X.B. Feng, J.Y. Zhang, Y.Q. Wang, Z.Q. Hou, K. Wu, G. Liu, J. Sun, Size
28 effects on the mechanical properties of nanocrystalline NbMoTaW refractory
29 high entropy alloy thin films, *Int. J. Plasticity* 95 (2017) 264-277.
- 30 [10] A.A. El-Aty, Y. Xu, S.-H. Zhang, S. Ha, Y. Ma, D. Chen, Impact of high strain
31 rate deformation on the mechanical behavior, fracture mechanisms and
32 anisotropic response of 2060 Al-Cu-Li alloy, *J. Adv. Res.* 18 (2019) 19-37.
- 33 [11] Y. Tang, D.Y. Li, Dynamic response of high-entropy alloys to ballistic impact,
34 *Sci. Adv.* 8 (2022) eabp9096.
- 35 [12] M. Rueda-Ruiz, B.D. Beake, J.M. Molina-Aldareguia, New instrumentation and
36 analysis methodology for nano-impact testing, *Mater. Des.* 192 (2020) 108715.
- 37 [13] G.I. G.T., F. P.S., Influence of peak pressure and pulse duration on
38 substructure development and threshold stress measurements in shock loaded
39 copperL, *Impact Loading and Dynamic Behavior of Materials 2*, DCM
40 Informationsgesellschaft Verlag (1988) 541-548.

- 1 [14] E. Hirscha, J. Plesekb, A theoretical analysis of experimental results of shock
2 wave loading of OFE copper relating the observed internal structure to the
3 deformation mechanism, *Int. J. Impact Eng.* 32(8) (2006) 1339-1356.
- 4 [15] A. Ghafarollahi, W.A. Curtin, Theory of kink migration in dilute BCC alloys,
5 *Acta Mater.* 215 (2021) 117078.
- 6 [16] S. NEMAT-NASSER, J.B. ISAACS, M. LIU, Microstructure of high-strain, high-
7 strain-rate deformed Tantalum, *Acta Mater.* 46(4) (1998) 1307-1325.
- 8 [17] G. Dirras, H. Couque, L. Liliensten, A. Heczcel, D. Tingaud, J.-P. Couzinié, L.
9 Perrière, J. Gubicza, I. Guillot, Mechanical behavior and microstructure of
10 Ti₂₀Hf₂₀Zr₂₀Ta₂₀Nb₂₀ high-entropy alloy loaded under quasi-static and
11 dynamic compression conditions, *Mater. Charact.* 111 (2016) 106-113.
- 12 [18] R.W. KLOPP, R.J. CLIFTON, T.G. SHAWKI, Pressure-shear impact and the
13 dynamic viscoplastic response of metals, *Mech. Mater.* 4 (1985) 375-385.
- 14 [19] Q. Wei, T. Jiao, K.T. Ramesh, E.Ma, Nano-structured vanadium: processing
15 and mechanical properties under quasi-static and dynamic compression,
16 *Scripta Mater.* 50(3) (2004) 359-364.
- 17 [20] S. Wei, E.S. Park, S.J. Kim, J. Kang, Y. Zhang, Y. Zhang, T. Furuwara, E.S.
18 Park, C.C. Tasan, Natural-mixing guided design of refractory high-entropy
19 alloys with as-cast tensile ductility, *Nat. Mater.* 19(11) (2020) 1175-1181.
- 20 [21] Y.F. Zhao, Y.Q. Wang, K. Wu, J.Y. Zhang, G.Liu, J. Sun, Unique mechanical
21 properties of Cu/(NbMoTaW) nanolaminates, *Scripta Mater.* 154 (2018) 154-
22 158.
- 23 [22] J.M. Wheeler, J. Dean, T.W. Clyne, Nano-impact indentation for high strain
24 rate testing: The influence of rebound impacts, *Extreme Mech. Lett.* 26 (2019)
25 35-39.
- 26 [23] M.R. Marulli, A. Valverde-González, A. Quintanas-Corominas, M. Paggi, J.
27 Reinoso, A combined phase-field and cohesive zone model approach for crack
28 propagation in layered structures made of nonlinear rubber-like materials,
29 *Comput. Method. in Appl. M.* 395 (2022).
- 30 [24] S. Maiti, W. Steurer, Structural-disorder and its effect on mechanical
31 properties in single-phase TaNbHfZr high-entropy alloy, *Acta Mater.* 106 (2016)
32 87-97.
- 33 [25] B. Song, Y. Li, Z. Cong, Y. Li, Z. Song, J. Chen, Effects of deposition
34 temperature on the nanomechanical properties of refractory high entropy
35 TaNbHfZr films, *J. Alloy. Compd.* 797 (2019) 1025-1030.
- 36 [26] I. Petrov, P. B. Barna, L. Hultman, J.E. Greene, Microstructural evolution
37 during film growth, *J. Vac. Sci. Technol. A* 21(5) (2003) S117-S128.
- 38 [27] B. Sboui, D. Rodney, P.-A. Geslin, Elastic modelling of lattice distortions in
39 concentrated random alloys, *Acta Mater.* 257 (2023) 119117.
- 40 [28] W.L. Wang, L. Hu, S.J. Yang, A. Wang, L. Wang, B. Wei, Liquid
41 supercoolability and synthesis kinetics of quinary refractory high-entropy alloy,
42 *Sci. Rep.-UK* 6 (2016) 37191.
- 43 [29] A. Zafari, K. Xia, Laser powder bed fusion of ultrahigh strength Fe-Cu alloys
44 using elemental powders, *Addit. Manuf.* 47 (2021).

- 1 [30] M.J. Bermingham, D.H. StJohn, J. Krynen, S. Tedman-Jones, M.S. Dargusch,
2 Promoting the columnar to equiaxed transition and grain refinement of titanium
3 alloys during additive manufacturing, *Acta Mater.* 168 (2019) 261-274.
- 4 [31] X. Shi, J. Chen, B.D. Beake, T.W. Liskiewicz, Z. Wang, Dynamic contact
5 behavior of graphite-like carbon films on ductile substrate under nano/micro-
6 scale impact, *Surf. Coat. Tech.* 422 (2021) 127515.
- 7 [32] K.M. Conway, C. Kunka, B.C. White, G.J. Pataky, B.L. Boyce, Increasing
8 fracture toughness via architected porosity, *Mater. Des.* 205 (2021) 109696.
- 9 [33] K. Komvopoulos, Finite element analysis of a layered elastic solid in normal
10 contact with a rigid surface, *J. Tribol.-T. ASME* 110 (1988) 477-485.
- 11 [34] P. Klose, V. Roddatis, A. Pundt, Tuning the stress state in Nb-thin films by
12 lateral size confinement, *Acta Mater.* 222 (2022) 117454.
- 13 [35] J. Chen, X. Shi, B.D. Beake, X. Guo, Z. Wang, Y. Zhang, X. Zhang, S.R.
14 Goodes, An investigation into the dynamic indentation response of metallic
15 materials, *J. Mater. Sci.* 51(18) (2016) 8310-8322.
- 16 [36] D. Tabor, *The Hardness of Metals*, Clarendon Press, Oxford, 1951.
- 17 [37] N.M. Jennett, J. Nunn, High resolution measurement of dynamic (nano)
18 indentation impact energy: a step towards the determination of indentation
19 fracture resistance, *Philos. Mag.* 91(7-9) (2011) 1200-1220.
- 20 [38] E.W. Andrews, A.E. Giannakopoulos, E. Plisson, S. Suresh, Analysis of the
21 impact of a sharp indenter, *Int. J. Solids Struct.* 39 (2002) 281-295.
- 22 [39] G. Constantinides, C.A. Tweedie, N. Savva, J.F. Smith, K.J.V. Vliet,
23 Quantitative Impact Testing of Energy Dissipation at Surfaces, *Exp. Mech.*
24 49(4) (2009) 511-522.
- 25 [40] R. Saha, Z. Xue, Y. Huang, W. Nix, Indentation of a soft metal film on a hard
26 substrate: strain gradient hardening effects, *J. Mech. Phys. Solids* 49 (2001)
27 1997-2014.
- 28 [41] K. Wang, N.R. Tao, G. Liu, J.Lu, K.Lu, Plastic strain-induced grain refinement
29 at the nanometer scale in copper, *Acta Mater.* 54(19) (2006) 5281-5291.
- 30 [42] A.A. Elmustafa, D.S. Stone, Indentation size effect in polycrystalline F.C.C.
31 metals, *Acta Mater.* 50 (2002) 3641-3650.
- 32 [43] M. Stefanelli, R. Daniel, W. Ecker, D. Kiener, J. Todt, A. Zeilinger, C. Mitterer,
33 M. Burghammer, J. Keckes, X-ray nanodiffraction reveals stress distribution
34 across an indented multilayered CrN–Cr thin film, *Acta Mater.* 85 (2015) 24-31.
- 35 [44] Y. IWAHASHI, Z. HORITA, M. NEMOTO, T.G. LANGDON, The process of
36 grain refinement in equal-channel angular pressing, *Acta Mater.* 46(9) (1998)
37 3317-3331.
- 38 [45] G.S. Rohrer, I. Chesser, A.R. Krause, S.K. Naghibzadeh, Z. Xu, K. Dayal,
39 E.A. Holm, Grain Boundary Migration in Polycrystals, *Annu. Rev. Mater. Res.*
40 53(1) (2023) 347-369.
- 41 [46] B.N. LUCAS, W.C. OLIVER, Indentation power-law creep of high-purity
42 Indium, *Metall. Mater. Trans. A* 30A 601-610.
- 43 [47] G.M. Pharr, E.G. Herbert, Y. Gao, The Indentation Size Effect: A Critical
44 Examination of Experimental Observations and Mechanistic Interpretations,

1 Annu. Rev. Mater. Res. 40(1) (2010) 271-292.

2 [48] P.M. Anderson, J.P. Hirth, J. Lothe, Theory of Dislocations, Cambridge
3 University Press, 2017.

4 [49] A.B.MANN, P.C.SEARSON, J.B.PETHICA, T.P.WEIHS, The relationship
5 between near-surface mechanical properties, loading rate and surface
6 chemistry, Mat. Res. Soc. Symp. Proc. 505 (1998) 307-318.

7 [50] A.A. Elmustafa, D.S. Stone, Nanoindentation and the indentation size effect:
8 kinetics of deformation and strain gradient plasticity, J. Mech. Phys. Solids 51
9 (2003) 357-381.

10